Geochemistry, Geophysics, Geosystems

RESEARCH ARTICLE
10.1029/2020GC009074

Key Points:

- Mn and Fe mineralogy, elemental composition, and average Mn redox state exhibit significant variability in a ferromanganese crust
- Mn undergoes significant increase in oxidation state, from +3.4 in new crust growth to +4.0 in the oldest sections
- Micro–X-ray absorption spectroscopy and micro–X-ray fluorescence reveal diagenetic characteristics in a ferromanganese crust

Supporting Information:

- Supporting Information 1

Correspondence to:
C. M. Hansel,
chansel@whoi.edu

Citation:
Sutherland, K. M., Wankel, S. D., Hein, J. R., & Hansel, C. M. (2020). Spectroscopic insights into ferromanganese crust formation and diagenesis. *Geochem Geophys Geosyst*, *21*, e2020GC009074. https://doi.org/10.1029/2020GC009074

Received 06 APR 2020
Accepted 23 OCT 2020

Spectroscopic Insights Into Ferromanganese Crust Formation and Diagenesis

Kevin M. Sutherland[1,2,3], Scott D. Wankel[1], James R. Hein[4], and Colleen M. Hansel[1]

[1]Department of Marine Chemistry and Geochemistry, Woods Hole Oceanographic Institution, Woods Hole, MA, USA, [2]Department of Earth, Atmospheric and Planetary Science, Massachusetts Institute of Technology, Cambridge, MA, USA, [3]Department of Earth and Planetary Science, Harvard University, Cambridge, MA, USA, [4]Pacific Coastal and Marine Science Center, U.S. Geological Survey, Santa Cruz, CA, USA

Abstract Marine ferromanganese deposits, often called the scavengers of the sea, adsorb and coprecipitate with a wide range of metals of great interest for paleo-environmental reconstructions and economic geology. The long (up to ~75 Ma), near-continuous record of seawater chemistry afforded by ferromanganese deposits offers much historical information about the global ocean and surface earth including crustal processes, mantle processes, ocean circulation, and biogeochemical cycles. The extent to which the ferromanganese deposits hosting these geochemical proxies undergo diagenesis on the seafloor, however, remains an important and challenging factor in assessing the fidelity of such records. In this study, we employ multiple X-ray techniques including micro–X-ray fluorescence, bulk and micro–X-ray absorption spectroscopy, and X-ray powder diffraction to probe the structural, compositional, redox, and mineral changes within a single ferromanganese crust. These techniques illuminate a complex two-dimensional structure characterized by crust growth controlled by the availability of manganese (Mn), a dynamic range in Mn oxidation state from +3.4 to +4.0, changes in Mn mineralogy over time, and recrystallization in the lower phosphatized portions of the crust. Iron (Fe) similarly demonstrates spatial complexity with respect to concentration and mineralogy, but lacks the dynamic range of oxidation state seen for Mn. Micrometer-scale measurements of metal abundances reveal complex element associations between trace elements and the two major oxide phases, which are not typically resolvable via bulk analytical methods. These findings provide evidence of post-depositional processes altering chemistry and mineralogy, and provide important geochemical context for the interpretation of element and isotopic records in ferromanganese crusts.

Plain Language Summary Ferromanganese crusts are mineral deposits found in all major ocean basins. These seafloor crusts slowly precipitate from seawater at a rate of millimeters per million years, reaching ages of up to about 75 million years. These deposits have received scientific and economic interest both because they contain chemical records of past ocean conditions, and because their valuable metal content make them potentially viable targets for deep-sea mining. In this study, using a representative crust from the Pacific Ocean, we compare sections of younger crust growth to older sections of crust to determine what changes occur over time that may affect metals of geologic and/or economic interest. We use several X-ray techniques to characterize changes in mineralogy, composition, and metal oxidation state. We found measurable changes in these properties throughout the crust, including changes in mineralogy, changes in element distribution with depth, and increasing oxidation state with increasing crust age. These results shed light on the processes controlling the formation and evolution of these globally ubiquitous and enigmatic deposits as well as emphasize that post-depositional changes should be considered and further explored when considering geologic records contained within ferromanganese crusts.

1. Introduction

Marine ferromanganese deposits, including both crusts and nodules, form in all five global ocean basins at almost every latitude (Cronan, 1977; Hein et al., 1997, 2000). Ferromanganese deposits have classically been categorized into one of three groups based on mode of formation and trace element associations: hydrogenetic deposits, diagenetic deposits, and hydrothermal deposits. Hydrogenetic ferromanganese deposits precipitate in direct contact with the water column on the surface of a substrate rock or existing crust or nodule

(Hein et al., 1997, 2000). The direct exposure of hydrogenetic ferromanganese crusts to ambient seawater and the tendency of iron (Fe) and manganese (Mn) oxy(hydr)oxides to (ad)sorb various metal(oid)s makes them valuable recorders of past ocean chemistry (Hein et al., 2000; Klemm et al., 2005; H. F. Ling et al., 2002; Nielsen et al., 2009; Sutherland et al., 2020; Wang et al., 2016). Diagenetic Fe-Mn nodules are distinct from hydrogenetic Fe-Mn deposits in that they form from the reduction and reprecipitation of elements such as Mn, copper (Cu), nickel (Ni), and lithium (Li) in sedimentary porewaters (Crerar & Barnes, 1974; Jung & Lee, 1999). If the sediment redox boundary is close enough to the seafloor, then those released metals can migrate upsection and contribute to the growth of Fe-Mn nodules on the seabed (Hein et al., 2020; Kuhn et al., 2017). Diagenetic nodules tend to grow at rates much faster than hydrogenetic Fe-Mn crusts (Jung & Lee, 1999; Von Stackelberg & Cronan, 2000). Hydrothermal Fe-Mn deposits occur near submarine hotspot volcanoes, volcanic arcs, and regions influenced by seafloor spreading. Deposits of hydrothermal origin tend to fall closer to pure Fe or Mn oxide endmembers and form as stratabound layers along the flow path of the hydrothermal fluid, giving them a distinct texture from hydrogenetic or diagenetic deposits (Hein et al., 1997, 2000). It is common to find nodules with compositions and/or morphologies reflecting two of these formation types, indicating the deposit formed in a transitioning environment (e.g., transition from purely hydrogenic to purely diagenetic nodules) or in an environment with intermediate character (i.e., mixed hydrothermal and hydrogenetic deposits where hydrothermal fluid enters the water column) (Bau et al., 2014).

While there are many compositional and morphological similarities between ferromanganese nodules and crusts, there are a few distinctions between their typical formation patterns and depositional environments. Nodules form by either hydrogenetic or diagenetic deposition on nucleation sites or as concentric layers on an existing nodule (Hein et al., 2000). Rock or mineral fragments, hard parts from animals such as bones or teeth, or even fragments from previous generations of nodules can serve as a nucleation site for a nodule (Hein et al., 2000). Fe-Mn nodules are most commonly found in deep marine environments below 4,000 m depth where sedimentation rates are typically below 10 mm ky^{-1} (Hein & Koschinsky, 2014). Seafloor coverage by ferromanganese nodules within the abyssal Pacific and Indian Ocean basins is estimated to exceed 50% in places (Rona, 2008). The abundance of seafloor Fe-Mn nodules declines below depths of 6,500 m. While the extent of coverage in the Atlantic and Artic Ocean basins is not fully characterized, documented occurrences of nodules in these two ocean basins appear to follow the same depth and sedimentation rate patterns observed for Pacific crusts (Hein et al., 2000; Hein & Koschinsky, 2014).

In contrast to nodules, Fe-Mn crusts form as layers coating hard-rock substrates. Fe-Mn crusts exhibit a much larger range of depositional depth and are typically observed between 400 and 7,000 m ocean depth, with the thickest Fe-Mn crusts occurring between 800 and 2,500 m (Hein & Koschinsky, 2014). Crusts occur with greater frequency and tend to reach greater thicknesses in the Pacific Ocean basin. Crusts observed in the Atlantic and Indian Ocean basins are in geographic proximity to the spreading centers that dominant those basins, and therefore tend to have more hydrothermal input than their Pacific counterparts (Hein et al., 2000). In contrast with nodules, crusts exhibit formation patterns and element compositions most consistent with hydrogenetic formation (Hein & Koschinsky, 2014). Fe-Mn crusts may also accumulate metals diffusing out of nearby sediment, although, this is thought to be quite rare (Hein et al., 1997, 2000, 2017). This type of diagenetic process based on redox cycling in the sediment to transfer metals to the crusts through enrichment in bottom waters should be distinguished from diagenetic reactions that may occur within crust layers. Phosphatization of the older parts of thick crusts is a well-known diagenetic process of the latter type that impacted crust formation during the middle Miocene and older times. Because Fe-Mn crusts are primarily hydrogenetic and not significantly influenced by sedimentary redox gradients and/or micro-environments, Fe-Mn crusts are viable candidates as hosts of basin-scale and global geochemical records.

Reliable dating techniques are a central aspect of Fe-Mn crust geochemistry important for contextualizing historical records contained within Fe-Mn deposits. Uranium series isotope ratios and cosmogenic beryllium-10 abundance are among those successfully used to date such deposits, but the window of applicability, approximately 10 Ma for Be isotopes and 400 ka for U-series, is less than the typical age for crusts (typically <75 Ma) (Frank, 2002; Marcus et al., 2015). Constant accumulation models of some elements have also been used to approximate Fe-Mn crust ages, but fall short in identifying periods of erosion or nondeposition

and secular changes in seawater chemistry (Conrad et al., 2017; Klemm et al., 2005). Stable osmium (Os) isotope ratios have been used for high-resolution age dating of samples up to 72 Ma, nearly 7 times what is achievable with Be-10 measurements (Klemm et al., 2005; Nielsen et al., 2009). Notably, however, some of the oldest observed Fe-Mn crusts exceed even this 70 Ma window (Klemm et al., 2005).

Fe-Mn crusts are passive recorders of changes in seawater chemistry that, in concert with calibrated age models, allow access to a wide range of paleo-environmental records (Banakar & Hein, 2000; Christensen et al., 1997; Dausmann et al., 2015; Frank et al., 2006; Frank & O'Nions, 1998; Horner et al., 2015; Klemm et al., 2005; Marcus et al., 2018; Nielsen et al., 2009). Analytical targets for paleo-records include proxies of Earth's crust and mantle processes, marine productivity, and other geochemical processes that produce variations in seawater chemistry. These studies, implicitly or explicitly, assume the Fe-Mn crust hosting these proxies are largely unaltered throughout their lifetime on the seafloor, with the exception of phosphatization by carbonate fluorapatite (CFA) in the older portions of many thick Pacific crusts. CFA precipitates in the pore spaces of older sections of Fe-Mn crusts, approaching 30 weight percent of the oldest sections of crusts from the Pacific, Atlantic, and Indian ocean basins (Hein et al., 2000).

Clearly, Fe-Mn crusts offer an important window into modern and past seawater chemistry, yet little is known about the post-depositional changes in the redox state, structure, and mineralogy of the host Fe-Mn minerals. In this study, we use micro–X-ray fluorescence (μ-XRF) and bulk and micro–X-ray absorption spectroscopy (μ-XAS) to obtain high-resolution maps of major and minor element distributions, Mn and Fe redox species, mineralogy, and primary and diagenetic textures within a well-studied hydrogenetic Fe-Mn crust from the Central Pacific Ocean (F7-86-HW CD29-2). These micrometer-scale resolution analyses highlight the complex nature of the structure of Fe-Mn crusts, as well as bring clarity and context to element distributions that are not resolvable with bulk analyses. Additionally, these measurements capture post-depositional changes undergone by a Fe-Mn crust on the surface of the seafloor over approximately 75 Myr.

2. Materials and Methods

2.1. Samples

F7-86-HW CD29-2 (hereafter referred to as CD29) is a hydrogenetic Fe-Mn crust collected from the Karin Ridge in the Central Pacific Ocean (16° 42′ N, 168° 14′ W) (Hein et al., 1990). CD29 was collected from approximately 2,000 m depth. An age model correlating the Os isotope stratigraphy of CD29 with that of pelagic clays suggests that the first ferromanganese layers of CD29 were deposited approximately 74 Ma atop basalt hyaloclastite (86 Ma) (Klemm et al., 2005; Nielsen et al., 2009). The oceanic crust underlying CD29 underwent tectonic shifts throughout the deposition of CD29. The deposition of CD29 began at about 1,000 m water depth, and its underlying oceanic crust has undergone approximately 1,000 m of thermal subsidence relative to sea-level (Horner et al., 2015). Over the same interval of time, the underlying oceanic crust of CD29 drifted by approximately 25 degrees from 10°S latitude to the latitude at which it was collected. The particular section of CD29 used in this study has a thickness of 105 mm, which was prepared in thin section using low-fluorescence EpoFix resin. Previous studies conducted on this particular crust include bulk element composition and mineralogy (Frank et al., 1999), osmium isotope stratigraphy (Klemm et al., 2005), and isotopes of lead, hafnium (Godfrey et al., 1997), iron (Horner et al., 2015), beryllium (von Blanckenburg et al., 1996), helium (Basu et al., 2006), thallium (Nielsen et al., 2009; Rehkämper et al., 2004), and many others.

2.2. X-ray Analyses

In this study, we used a range of X-ray techniques including XAS, XRF, and X-ray diffraction (XRD). XAS techniques included X-ray absorption near edge structure (XANES) and extended X-ray absorption fine structure (EXAFS), which are used to characterize metal oxidation state and metal bonding environment, respectively. Micro-XRF maps the abundance and distribution of major elements within the crust. XRD determines the spatial orientation of diffraction reflections within minerals, and thus the mineral structure. The application of these techniques on various spatial scales within the ferromanganese crust provides a

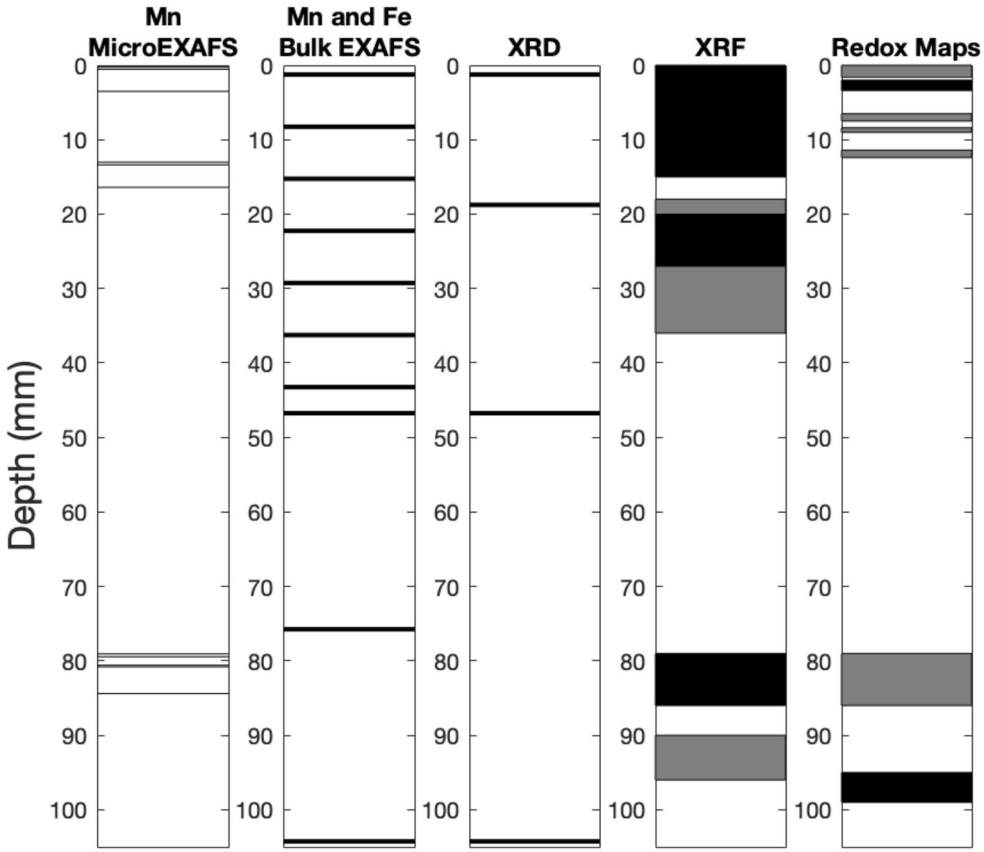

Figure 1. Diagram of data collected as part of this study. Black lines and boxes indicate the approximate depths of individual analyses conducted. Gray boxes indicate data provided in the supporting information.

comprehensive picture of how the composition, mineralogy, and redox structure vary over the history of the crust.

Bulk XAS, μ-XAS, and μ-XRF were conducted at Stanford Synchrotron Radiation Lightsource (SSRL) on beamlines 4-3, 2-3, 10-2, and 14-3. Bulk XANES and EXAFS were collected for Mn and Fe on sub-samples of CD29 that were drilled from 10 depths throughout the crust to capture the redox and mineralogical trends within the crust (Figure 1). Samples were housed in a liquid nitrogen cooled apparatus during data collection to inhibit incidental metal photoreduction. Comparison of the edge position of multiple scans indicated undetectable beam damage during spectral collection. XANES and EXAFS spectra were fit using the SIXPACK Software package (Webb, 2005). Mn XANES spectra were fit with δ-MnO_2 (synthetic analog of vernadite), feitknechtite (MnOOH), and $MnCl_2$, as Mn(IV), Mn(III), and Mn(II) end-members, respectively. Fe XANES spectra were fit with synthetic 2-line ferrihydrite and siderite as Fe(III) and Fe(II) end-members, respectively. Mn EXAFS spectra were fit over a *k* range of 1–12 with standard spectra including δ-MnO_2, acid- and sodium-birnessites (general formula for birnessite group minerals: $(Na,Ca,K)_{0.6}(Mn^{4+},Mn^{3+})_2O_4{\cdot}1.5H_2O$), feitknechtite (MnOOH), groutite (MnOOH), hausmannite (Mn_3O_4), todorokite $(Ca,Na,K)_x(Mn^{4+},Mn^{3+})_6O_{12}{\cdot}3.5H_2O$, aqueous $MnSO_4$, pyrolusite (MnO_2), asbolane $(Mn(O,OH)_2(Ni,Co)_x(O,OH)_2{\cdot}nH_2O)$, and rhodochrosite ($MnCO_3$) (Bargar et al., 2005; Learman et al., 2011; Manceau et al., 1992b; Post, 1999; Villalobos et al., 2003; Webb et al., 2005). Fe EXAFS were fit over a *k* range of 1–11 with a standard database that contained a broad range of Fe-bearing minerals including silicates, oxides, sulfides, and carbonates. After an initial survey was conducted to rule out several standards in the database, EXAFS standard spectra were further refined to the following subset of phases: 2-line ferrihydrite ($Fe(OH)_3{\cdot}nH_2O$), aluminum-substituted ferrihydrite, feroxyhyte (FeOOH), goethite (FeOOH), hematite (Fe_2O_3), siderite ($FeCO_3$), Fe-rich biotite $(K(Mg,Fe)_3(AlSi_3O_{10})(OH)_2)$,

Fe-rich smectite ($Mg_{0.4}(Fe^{3+}_{1.5}Mg_{0.4}Ni_{0.1})(Si_{3.7}Al_{0.3}O_{10})(OH)_2$), green rust sulfate ($Fe^{2+}_{6-x}Fe^{3+}_x(OH)_{12}(SO_4)_{x/2}$), lepidocrocite (FeOOH), and magnetite (Fe_3O_4) (Das et al., 2011; Hansel et al., 2003, 2004). It is important to note that we recognize that the fits presented are only as good as the standards used to fit them, and that the mineralogy of ferromanganese crusts is exceedingly complex. Although we include a significant number of relevant phases for which endmember reference phases are available, we recognize that this may not be exhaustive, and therefore may not capture all of the mineralogical complexity in this sample.

Micro-XRF maps of several metals of interest within CD29 were collected at 11,000 eV (Mn, Fe, Co, Cu, Ni, Ti, and Zn) and 4,090 eV (Si) on beamlines 2-3 and 14-3, respectively. Mn and Fe redox maps were collected using beamline 2-3 using multiple-energy mapping. This technique involves collecting several 2-D maps of an area of interest at several different energies surrounding the absorption edge of the element of interest (Farfan et al., 2018; Mayhew et al., 2011). For Mn, multiple-energy maps were collected at 6,553, 6,559, 6,562, and 6,570 eV (Hansel et al., 2012). For Fe, multiple-energy maps were collected at 7,122, 7,124, 7,126, 7,128, and 7,130 eV (Mayhew et al., 2011). For each set of multiple energy maps, we performed a principal component analysis (PCA) using the SIXPACK Software Package to identify regions of the greatest difference among the multiple-energy maps (Webb, 2005). Several reference (XANES) spectra were collected in each distinct region of the multiple-energy maps. We performed PCA on the XANES spectra (typically >20 distinct points for each region of interest) to determine the minimum number of XANES spectra required to describe the variation among each set of multiple energy maps. To avoid any influence of self-absorption on the fitting of each redox end-member and the multiple energy map, we used the self-absorption correction routine available in SIXPACK (Webb, 2005). Due to the close proximity of the Fe K-beta and Co K-alpha emission energies, the two peaks were deconvolved using the Gaussian fitting routine provided in the MicroAnalysis Toolkit software package (Webb, 2011).

To further explore how Mn redox and mineral variability within the Fe-Mn crust related to individual growth features within the crust, we conducted Mn micro EXAFS (μ-EXAFS) spectroscopy. μ-EXAFS spectra were collected at SSRL on beamline 10-2 with a Si(220) monochrometer ($\Phi = 90°$) and a 30-micron beam size. For sample locations that required multiple scans, the beam position was slightly offset to avoid beam-induced photoreduction. Mn μ-EXAFS spectra were fit with the same suite of Mn mineral standards listed above. Any standard with a calculated contribution of 5% or less (the previously defined detection limit for this method [Bargar et al., 2000]) to the EXAFS spectra was omitted from the fit and refit iteratively with the remaining components. While the EXAFS fits we present are quantitative, they are limited by the model compounds within the spectral library. Thus, in order to further evaluate mineralogical heterogeneity, we also combined EXAFS with XRD analysis. We collected multiple X-ray powder diffraction patterns from discreet sections throughout the crust for comparison with EXAFS measurements (Rigaku Rapid II, Mo source, 0.3 mm collimator, λ = 0.70930Å). Samples were mounted on a Kapton tip with mineral oil and run for 20–30 min with omega fixed and phi rotating at 1 degree per second. Two-dimensional diffraction images were background corrected (manual setting of 5) and intensity integrated using the 2DP software package.

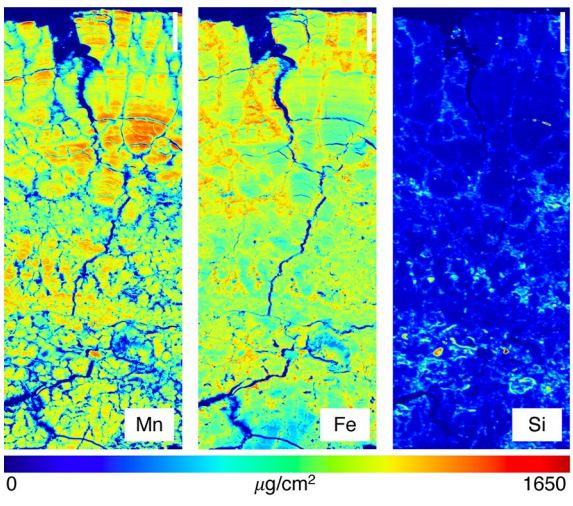

Figure 2. Micro–X-ray fluorescence images of Mn, Fe, and Si of the topmost section of crust CD29. Mn concentrations are highest within individual growth columns, while Fe and Si concentrations are highest in the areas between columns and in material filling cracks. Scale bar (top right) represents 1 mm.

3. Results

3.1. Element Composition

Figure 2 shows the element distribution of the topmost section (0–10 mm) of crust CD29 for the three most abundant cations: Mn, Fe, and Si (Ti, Co, Ni, Cu, and Zn images of the same region is provided in the supplement). These images demonstrate that CD29 is composed of growth columns ranging in size from hundreds of microns to several millimeters within a ~10 mm-thick section; the columnar sections alternate with 1–2 mm-thick mottled sections. The center of the columns is dominated by Mn, with the highest Fe and Si is found between the

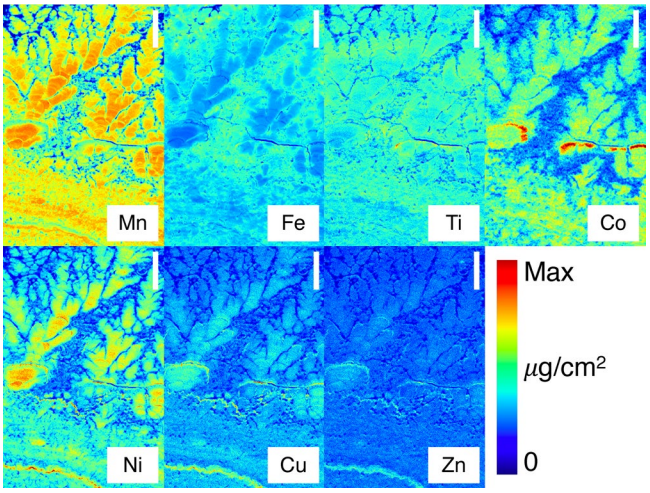

Figure 3. Micro–X-ray fluorescence images of a representative section of ferromanganese growth structures (branching columns; laminations) in the upper section of the crust. Max concentrations are 1,350 μg/cm^2 (Mn and Fe), 100 μg/cm^2 (Ti), 50 μg/cm^2 (Co), 30 μg/cm^2 (Ni), and 10 μg/cm^2 (Cu and Zn). Scale bar (top right) represents 1 mm.

columns, which is typical of hydrogenetic crusts—the columns are separated during growth by detrital silica and silicate grains cemented by predominantly Fe oxides. In Figure 3, we present a more detailed look at one set of Fe-Mn branched growth columns at 20 mm depth (just below Figure 2), including major and minor element concentrations of Mn, Fe, Ti, Co, Ni, Cu, and Zn (μ-XRF at 11 keV); this branched columnar section is underlain by a laminated section composed of acicular, massive, and mottled laminae. Further down in the crust (79 mm), where CFA fills in the pore space of CD29 (~10 wt%, Frank et al., 1999), these columnar-laminated fabrics give way to a less porous fabric with distinct compositional banding parallel to the growth plane of the crust (Figure 4).

Correlations for the elements in Figures 2 and 4 are provided in Table 1 (n > 400,000 pixels in both images). We note that values presented in Table 1 are not directly comparable to correlation matrices based on total element concentrations from bulk analysis presented elsewhere (Frank et al., 1999); the presence of cracks and metal poor regions in the crust mean that element correlations are not normalized to mass. Co, Cu, Ni are predominately correlated with Mn over Fe (Co: R^2 = 0.47 upper, 0.29 lower, Cu: R^2 = 0.53 upper, 0.45 lower; Ni: R^2 = 0.82 upper, 0.57 lower) (Figures 3 and 4; Table 1). Ti and Zn exhibit more complex behavior. Ti is positively correlated with both Fe (R^2 = 0.47) and Mn (R^2 = 0.53) in the topmost portion of the crust, but the Ti-Mn relationship becomes much weaker with depth (R^2 = 0.18). Zn has a weak positive correlation that decreases with depth with both Mn (R^2 = 0.37 upper, 0.20 lower) and Fe (R^2 = 0.30 upper, 0.11 lower).

3.2. Bulk XAS

Bulk Mn and Fe XANES and EXAFS are shown in Figures 5 and 6, with quantitative fit results and reduced chi-square statistic for each fit shown in Tables 2–5. Mn appears to have multiple trends in mineral character and redox state with depth (age) in the crust. The proportion of δ-MnO_2 within the EXAFS fits starts at 22% in the first sampled interval, increasing with depth to >75% near the bottom of the crust (Table 3). Acid birnessite, feitknechtite, and asbolane spectra at the first sampled interval contribute 18%, 24%, and 36%, respectively. We also found that todorokite produced an acceptable fit in place of feitknechtite, resulting from the similarity of several Mn-oxide EXAFS spectra. High-surface todorokite that decreases with depth is at odds with the general understanding that it may only be a minor diagenetic phase in phosphatized ferromanganese crust layers (Hein & Koschinsky, 2014). Todorokite (and 10 Å phases generally) is thought to be rare in hydrogenetic Fe-Mn crusts, and is found in less than 5% of crust samples (Hein et al., 2000). Todorokite may also be a minor phase in ferromanganese nodules (Kuhn et al., 2017; Wegorzewski & Kuhn, 2014). Therefore, in this case we omitted todorokite from the fit library. The fractional contribution of feitknechtite decreases with increasing depth in the crust, while birnessite and asbolane remain present throughout most of the crust. XANES data reveal that these general trends in mineralogy occur in parallel with an overall increase in Mn oxidation state with increasing depth into the crust, with the youngest section having an average Mn oxidation state of 3.46, and the oldest having an average Mn oxidation state of 3.91 (Table 2). Typical error for Mn redox states collected in this way is <3% (Bargar et al., 2005).

Iron EXAFS and XANES reveal different trends in mineralogy and redox state than those observed for Mn. Feroxyhyte and ferrihydrite are the primary components at all depths (Table 5), with intermittent contributions from more crystalline oxides, goethite and hematite, and Fe-rich clay minerals. Iron was near +3 valence at all sample depths (Table 4). Two samples demonstrated a small (~2%) Fe(II) component, but this is most likely within error and at the detection limit.

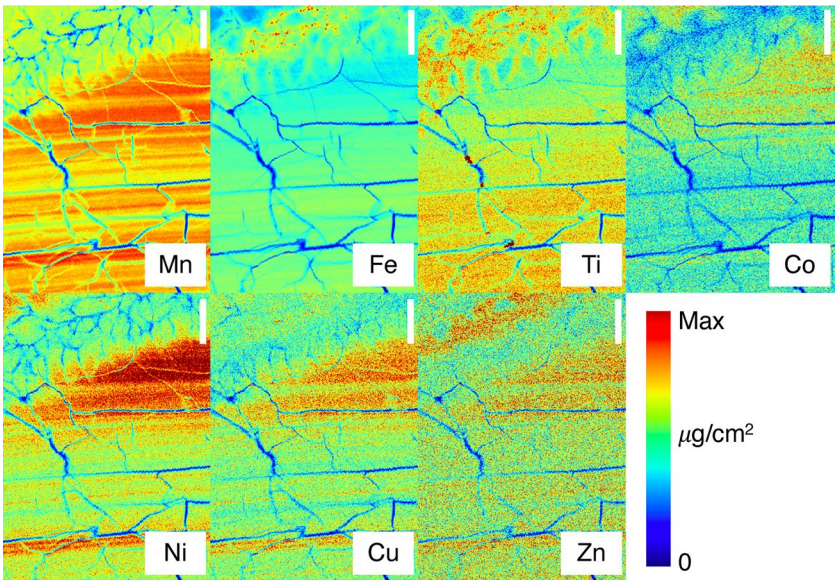

Figure 4. Micro–X-ray fluorescence images of a representative parallel laminated section of the lower, phosphatized section of the crust and overlying micro-columnar layer. Max concentrations are 1,650 μg/cm^2 (Mn and Fe), 100 μg/cm^2 (Ti), 50 μg/cm^2 (Co), 30 μg/cm^2 (Ni), and 10 μg/cm^2 (Cu and Zn). Scale bar (top right) is 1 mm.

3.3. μ-EXAFS

Manganese μ-EXAFS spectra collected at several depths throughout the crust are shown in Figure 7. These spectra include representatives of the most recent growth, crust growth older than 50 Ma, specific growth structures, and space between growth structures. Several standards were used to fit these μ-EXAFS spectra (see Materials and Methods), but only model compounds with >5% contribution to any sample are shown in Figure 7. Table 6 shows the component fits for each standard and a description of the location in which the spectrum was collected. Samples in the topmost portion of CD29 demonstrate Mn in bonding environments similar to a mixture of the spectral standards birnessite (include hexagonal and triclinic), feitknechtite, and asbolane. At greater crust depths, δ-MnO_2, asbolane, and birnessite components represent the greatest fractional contributions to CD29 EXAFS spectra, with some laminae with feitknechtite.

Table 1
R^2 of Elements in CD29 Measured by Micro–X-ray Fluorescence for Stratigraphic Sections Shown in Figures 2 and 4 (n > 400,000 Pixels)

	Mn	Fe	Zn	Cu	Ti	Co	Ni
				Figure 3			
Mn	1	0.182	0.368	0.534	0.528	0.465	0.822
Fe	-	1	0.298	0.161	0.467	0.067	0.108
Zn	-	-	1	0.355	0.374	0.107	0.324
Cu	-	-	-	1	0.365	0.214	0.542
Ti	-	-	-	-	1	0.270	0.402
Co	-	-	-	-	-	1	0.439
Ni	-	-	-	-	-	-	1
				Figure 4			
Mn	1	0.248	0.201	0.452	0.181	0.286	0.575
Fe	-	1	0.110	0.054	0.468	0.025	0.011
Zn	-	-	1	0.139	0.063	0.068	0.149
Cu	-	-	-	1	0.040	0.194	0.425
Ti	-	-	-	-	1	0.015	0.017
Co	-	-	-	-	-	1	0.275
Ni	-	-	-	-	-	-	1

3.4. XRD

XRD measurements were collected on four bulk samples (each representing approximately 2.5 mm of crust growth) from throughout the crust, including two samples in the upper, unphosphatized section of the crust (surface scrape and 17.5–20 mm), and two samples in the lower, phosphatized section of the crust (48.5–51 mm and the bottom of the crust) (Figure 8). All sections of the crust exhibited broad XRD reflections at 2.46 Å and 1.45 Å d-spacing, characteristic of vernadite (Post, 1999). Reflections corresponding to CFA were observed in the two samples in the lower phosphatized section of the crust. We did not observe 7 Å or 10 Å peaks in the diffraction pattern of CD29, which are characteristic of typical phyllomanganate (e.g., birnessite group minerals, buserite, and asbolane) and todorokite. No discernable Fe phases were seen in the diffraction patterns. A small peak was observed close to 3.3 Å, which we infer to be the most prominent diffraction of quartz. Quartz has been shown to be present as a minor component of CD29 (1%–2%) (Frank et

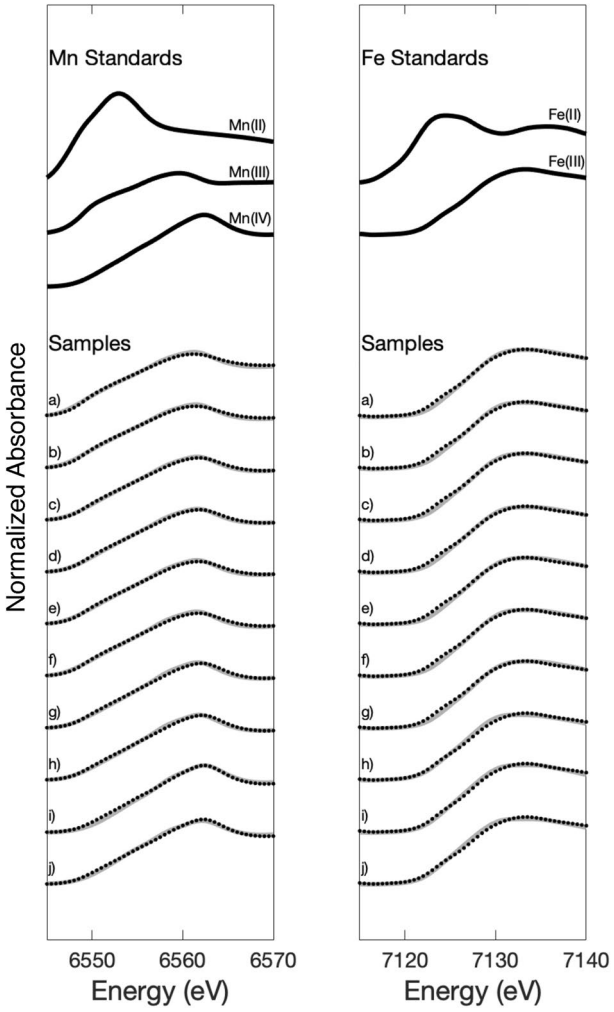

Figure 5. Mn and Fe XANES spectra and fits for bulk XANES analysis. δ-MnO_2, feitknechtite, and $MnCl_2$ were used for Mn redox standards, ferrihydrite and siderite were used for Fe redox standards. The raw data are plotted in gray, the least-squares fits of each spectrum is plotted on top of the data in black dotted line. Depths from the top of the crust (a) through (j) correspond to the following: 0–2.5, 7–9.5, 14–16.5, 21–23.5, 28–30.5, 35–37.5, 42–44.5, 45.5–48, 74.5–77, and 102.5–105 mm

al., 1999; Hein et al., 1990). Other less-prominent quartz peaks are not visible due to low abundance.

3.5. Mn and Fe Redox Maps

Maps of Mn and Fe oxidation states are shown in Figure 9. For Fe and Mn, two spectra were sufficient to describe >99% of the variation observed within the multiple energy maps. Using XANES fitting, we determined these two endmembers to be the most oxidized and most reduced examples of each metal in the sample. For Mn, these oxidation state endmembers were +3.4 and +4.0, and for Fe these endmembers were +2.8 and +3.0. Average Mn oxidation state tends to increase going outward from the center to the edge of columnar growth structures and going lower in ferromanganese crust stratigraphy. Average Fe oxidation state showed similar structural trends, with edges being the most oxidized. There was no significant Fe oxidation state trend with depth in the crust. These results largely agree with the redox trends determined via bulk XANES (Tables 2 and 4).

4. Discussion

4.1. Primary Crust Features

Ferromanganese crusts have a defined start and end, with a clear sense of time between them. This application of Steno's principles guides us in our interpretation as to the primary and diagenetic features of the Fe-Mn crust investigated here. The most recent growth features of CD29 are laminated columnar growth structures that vary in scale from 100 μm to several mm (Figure 2). In general, individual growth features tend to have the highest Mn concentrations in their interior, with Mn concentrations decreasing toward the margin of growth columns. Fe concentration tends to vary inversely with Mn within these individual growth features. These findings demonstrate a strong relationship between composition and growth structure in the ferromanganese crust. The center of each growth column has Mn:Fe ratios greater than 1, suggesting the nucleation of new crust growth is in large part controlled by the availability and/or the oxidation of Mn, which are reflected in the growth rates.

Columns contrast with the interstitial space between columns that have the highest concentrations of Fe, and correspondingly low Mn:Fe ratios. This distribution of Fe suggests that Fe minerals occur as both a co-precipitate with Mn oxides (high Mn:Fe) and as a cement for detritus-rich phases deposited by fluid flow around primary growth columns (lower Mn:Fe). This interstitial space also hosts the majority of Si-bearing material. The texture of Si in CD29 is consistent with detrital silica (quartz) and silicate minerals (feldspar and clay minerals) and bio-opal. Phillipsite, a zeolite mineral, has been observed in a number of marine Fe-Mn deposits (Hein et al., 2000), but we could not positively identify such a phase in our measurements although it was detected in other crusts from the same ridge where CD29 was collected (Hein et al., 1990). A quartz peak at 3.3 Å (Figure 8) was the only discernable feature in XRD that allows for the positive identification of a silica phase, although previous work demonstrated plagioclase feldspar is also clearly present (Frank et al., 1999; Hein et al., 1990). The intermittent presence of Fe-smectite in bulk EXAFS fits points to detrital incorporation of clay minerals.

Several first-row transition metals analyzed in this study (Co, Zn, Ni, Cu, and Ti), exhibit complex behavior in how they partition among the various mineral phases present in these crusts (Bodei et al., 2007; Manceau et al., 2003; Manceau et al., 1992a, 1992b, 2007a, 2007b; Peacock & Sherman, 2007; Takahashi et al., 2007).

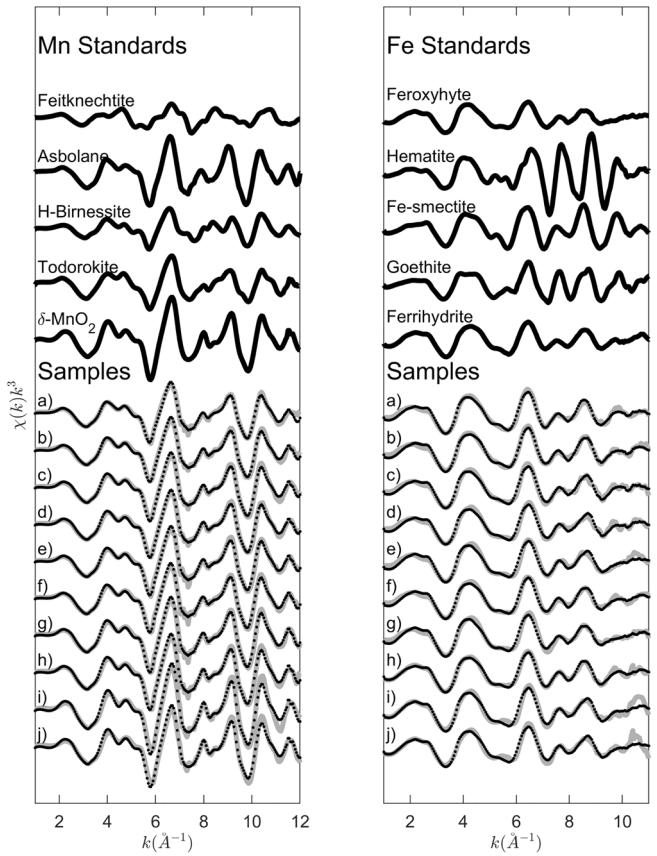

Figure 6. Mn and Fe EXAFS spectra and fits for bulk EXAFS analysis. Each included standard was determined to contribute >5% to the least squares fit of each EXAFS spectrum. The raw data are plotted in gray, the least-squares fits of each spectrum is plotted on top of the data in black dotted line. Depths (a) through (j) correspond to the following: 0–2.5, 7–9.5, 14–16.5, 21–23.5, 28–30.5, 35–37.5, 42–44.5, 45.5–48, 74.5–77, and 102.5–105 mm.

Surface sorption followed by incorporation into the mineral structure and diagenetic change mediate these relationships, and are in large part directed by the formation environment of a given deposit (e.g., hydrogenetic, diagenetic, or hydrothermal) (Bodei et al., 2007; Manceau et al., 2003, 2007a; Peacock & Sherman, 2007). Typically, elements exhibit patterns of association with major phases in bulk Fe-Mn crusts. Co, Zn, and Ni are typically associated with the Mn-oxide phase, whereas Cu and Ti are typically associated with Fe oxide (Hein & Koschinsky, 2014; Manceau et al., 1992a, 1992b, 2007b; Marcus et al., 2015). Our μ-XRF mapping allows for insights into these trace co-precipitation associations that bulk analyses do not. Indeed, our observations demonstrate correlations of Ni, Co, and Cu tend to correlate better with Mn than Fe. These methods also demonstrate the complex nature of elements like Ti and Zn. For example, Ti has a moderate positive correlation with Mn in the topmost section of CD29 ($R^2 = 0.53$), but this relationship gets much weaker with depth and age ($R^2 = 0.18$), while the correlation between Fe and Ti does not change significantly. In the younger portions of the crust, the Zn distribution appears similar to that of Mn (Figure 3). In the older portions of the crust, however, Zn concentrations are highest in the regions with highest Mn and Fe (Figure 4). This is consistent with previous work demonstrating that Zn in Fe-Mn nodules from soil partitions among several phases including goethite, birnessite, and phyllosilicates (Manceau et al., 2003), as it does with marine Fe-Mn crusts (Koschinsky & Hein, 2003). Such diverse metal associations within a single Fe-Mn crust should be considered, for example, when interpreting isotopic records (and isotope fractionation between aqueous phase and different mineral phases) contained within them.

There has been much speculation about the role of microbes in the formation and growth of Fe-Mn deposits. Indeed, the surface of a Fe-Mn nodule was shown to host dense communities of bacteria and archaea (Blöthe et al., 2015; Shiraishi et al., 2016). The growth patterns of CD29 are reminiscent of stromatolites (Bosak et al., 2013), and microbial Mn oxidation has been demonstrated across disparate groups of eukaryotes and bacteria that produce Mn(II)-oxidizing enzymes and reactive oxygen species (Geszvain et al., 2012; Hansel, 2017; Hansel et al., 2012;

Table 2
Bulk Mn X-ray Absorption Near Edge Structure (XANES) Fitting Results

Depth in CD-29 (mm)	Mn XANES component fits (fraction)			Average oxidation state	χ_v^2
	Mn(IV) (δ-MnO_2)	Mn(III) (Feitknechtite)	Mn(II) ($MnCl_2$)		
0–2.5	0.462	0.538	-		3.46
7–9.5	0.515	0.485	-	3.51	0.0003
14–16.5	0.615	0.385	-	3.62	0.0002
21–23.5	0.638	0.362	-	3.64	0.0002
28–30.5	0.608	0.392	-	3.61	0.0002
35–37.5	0.605	0.395	-	3.61	0.0003
42–44.5	0.753	0.247	-	3.75	0.0004
45.5–48	0.794	0.206	-	3.79	0.0003
74.5–77	1.000	0.000	-	4.00	0.0008
102.5–105	0.910	0.090	-	3.91	0.0005

Table 3
Bulk Mn Extended X-ray Absorption Fine Structure (EXAFS) Fitting Results

	Mn EXAFS component fits (fraction)					
Depth in CD-29 (mm)	δ-MnO_2	Acid birnessite	Sodium birnessite	Feitknechtite	Asbolane	χ_ν^2
0–2.5	0.217	0.184	-	0.243	0.357	
7–9.5	0.382	0.168	-	0.165	0.285	0.194
14–16.5	0.434	0.210	-	0.091	0.264	0.216
21–23.5	0.444	0.176	-	0.125	0.255	0.151
28–30.5	0.398	0.163	-	0.131	0.308	0.207
35–37.5	0.283	0.242	-	0.089	0.386	0.194
42–44.5	0.404	0.181	-	0.083	0.332	0.218
45.5–48	0.473	0.179	-	0.071	0.278	0.292
74.5–77	1.000	-	-	-	-	0.789
102.5–105	0.947	0.053	-	-	-	0.586

Hansel & Learman, 2015; Learman et al., 2011a; Sutherland et al., 2018; Tang et al., 2013; Tebo et al., 2004, 2005). Furthermore, the dominant Mn oxide formed by microbes is a hexagonal birnessite phase similar in structure to δ-MnO_2, the dominant phase identified within the crusts (Bargar et al., 2005; Grangeon et al., 2010; Jürgensen et al., 2004; Learman et al., 2011b; Santelli et al., 2011; Toner et al., 2006; Villalobos et al., 2006; Webb et al., 2005). These growth textures and oxide structures, however, are not necessarily microbial, and may result from abiotic, stochastic, and/or surface-normal growth processes (Grotzinger & Rothman, 1996). At most, Mn oxidation may control the nucleation and growth of Fe-Mn crusts, which in turn may be regulated by microbial activity, either directly or indirectly. We can only conclude that Mn-rich growth columns and crust texture are consistent with, but not necessarily indicative of, microbially mediated Mn oxidation.

The average Mn oxidation state in CD29 is dynamic even within the primary growth features in the topmost section. The topmost layers of CD29 growth columns contain Mn in the lowest average redox state exhibited in the crust: +3.4. Similar mixed valance Mn-oxides have been observed on the outer rim of one ferromanganese nodule (Blöthe et al., 2015; Shiraishi et al., 2016), but this is not necessarily true for all nodules (Johnson et al., 2016). The Mn oxidation state in CD29 increases toward the edge of growth column structures, which shows a maximum of ~3.7 (Figure 9). This small-scale dynamic redox texture has implications for element associations and geochemical records of redox-active elements and isotopes. Redox-active elements incorporate into the Fe-Mn crusts through oxidative sorption coupled with Mn reduction

Table 4
Bulk Fe X-ray Absorption Near Edge Structure (XANES) Fitting Results

	Fe XANES component fits			
Depth in CD-29 (mm)	Fe(III) ferrihydrite	Fe(II) siderite	Average oxidation state	χ_ν^2
0–2.5	1.000	-		3.000
7–9.5	1.000	-	3.000	0.0006
14–16.5	1.000	-	3.000	0.0007
21–23.5	1.000	-	3.000	0.0005
28–30.5	1.000	-	3.000	0.0008
35–37.5	1.000	-	3.000	0.0007
42–44.5	1.000	-	3.000	0.0008
45.5–48	0.981	0.019	2.981	0.0008
74.5–77	1.000	-	3.000	0.0006
102.5–105	0.982	0.018	2.982	0.0009

Table 5
Bulk Fe Extended X-ray Absorption Fine Structure (EXAFS) Fitting Results

	Fe EXAFS component fits					
Depth in CD-29 (mm)	Fe-smectite	Goethite	Hematite	Ferrihydrite	Feroxyhyte	χ_ν^2
0–2.5	0.189	-	-	0.287	0.524	
7–9.5	-	0.118	-	0.704	0.179	0.224
14–16.5	0.102	-	0.064	0.404	0.430	0.308
21–23.5	-	-	0.080	0.584	0.336	0.334
28–30.5	-	-	0.067	0.394	0.539	0.393
35–37.5	-	0.118	-	0.503	0.378	0.240
42–44.5	-	-	-	0.294	0.706	0.321
45.5–48	0.150	0.095	-	0.237	0.519	0.167
74.5–77	-	-	0.070	0.485	0.445	0.639
102.5–105	-	-	0.087	0.493	0.420	0.616

(Nielsen et al., 2013; Ohta & Kawabe, 2001; Peacock & Moon, 2012); the range of the average Mn redox state demonstrates the ability for Mn to facilitate oxidative sorption that may vary spatially and temporally. Unlike Mn, Fe demonstrates very little redox structure throughout the crust.

Bulk Fe EXAFS show the primary Fe-bearing phases are ferrihydrite and feroxyhyte. We also detected several occurrences of Fe-bearing clay and more crystalline Fe (hydr)oxide phases. The primary Mn phases as determined by bulk EXAFS are consistent with a mixture of the disordered hexagonal birnessite phase vernadite (as identified via the synthetic analog δ-MnO_2), acid birnessite (hexagonal), asbolane, and feitknechtite (Mn(III) oxyhydroxide). We note that feitknechtite is typically observed to form under conditions with much higher Mn(II) than is often observed in bottom waters (Elzinga, 2011). Mechanistically, feitknechtite can form by surface-catalyzed reaction of sorbed Mn(II) on a phyllomangate such as birnessite (Elzinga, 2011). It is possible that feitknechtite formed in pore space micro-environments with elevated aqueous Mn(II) concentrations. Further, there is growing recognition that Mn(III) can comprise a significant fraction of dissolved Mn in porewaters and the marine water column (Madison et al., 2013; Oldham et al., 2017). The influence of dissolved Mn(III) on Mn oxide phase formation has not been explored. It is also possible that feitknechtite may share spectral similarities with other Mn(III) oxyhydroxides not present in our library. In any case, the evidence indicates the presence of a Mn(III) oxyhydroxide mineral, which is most abundant in the youngest layers of crust. The heterogeneity in Mn mineralogy is further illuminated by the μ-EXAFS results, which identify a mixture of acid-birnessite (hexagonal), sodium birnessite (triclinic), feitknechtite, and asbolane. In order sections of crust, this assemblage is similar to the mixture of components observed in the bulk EXAFS. We note that the XRD results are somewhat at odds with our EXAFS results in that the diffraction pattern does not show clear evidence of either a 7 or 10 Å d-spacing, which would be expected for birnessite group minerals and asbolane. We discuss this finding in detail in the following section.

4.2. Diagenesis

High-resolution, two-dimensional analyses of Fe-Mn crust element distributions offer insight into changing element correlations with age. Some elements (e.g., Ni) show a strong preference for a given mineral phase, but many of these associations in the older crust become stronger with time. Some elements, such as Ti, Zn, and Co (Figures 3, S1, and S2), demonstrate pronounced horizontal bands, perhaps indicative of secular variation in the bottom-water abundance of these metals relative to Fe and Mn. In addition, diagenetic changes within the crust may explain some of this compositional variability through time. A feature suggesting that diagenesis does play a role in such compositional changes is seen in Figure 4. This figure demonstrates laminae parallel to the plane of growth (older) that give way to a more porous columnar growth features in younger crust. This textural change, which occurs in the phosphatized section of CD29 (>80 mm, >50 Ma) is symptomatic of post-depositional processes in which dissolution and reprecipitation

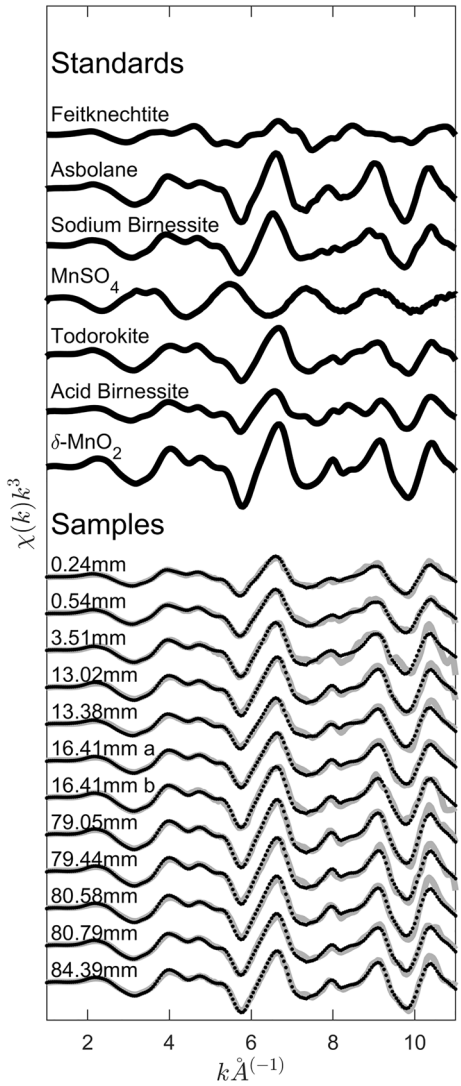

Figure 7. μ-EXAFS spectra of Mn in the ferromanganese crust CD29. Each included standard was determined to contribute >5% to the least squares fit of each EXAFS spectrum. The depth of each sample is listed. Description of each sample location is provided in Table 6.

remobilizes and repartitions Mn, Fe, and associated metals. Similar observations have been previously reported, concluding that suboxic conditions may have facilitated partial dissolution and reprecipitation of more stable phases (Koschinsky et al., 1997; Puteanus & Halbach, 1988; Wegorzewski et al., 2020). This partial repartitioning of elements is apparent in chemical changes documented in Table 1 as well.

Bulk Mn XAS reveals post-depositional oxidation and mineralogical changes with increasing depth in CD29. The Mn oxidation state of the youngest crust (+3.4), is much less oxidized than the oldest crust (+4.0); this range is well beyond the detection limit of Mn XANES (Bargar et al., 2000). Unlike younger crust growth, the oldest crust does not show a relationship between Mn oxidation state and major growth features. While there are some slight Fe redox changes between the center and edge of growth structures, the dynamic range is less than 0.1 oxidation state, differences that are likely unresolvable using this method.

The changes in Mn redox state (Table 2, Figure 9) are consistent with primary precipitation of mixed-valance oxides, including the Mn(I-II) oxyhydroxide feitknechite, followed by oxic diagenesis. Primary, mixed-valance Mn oxides are commonly seen in laboratory settings, including Mn oxides produced by bacteria and fungi (Grangeon et al., 2010; Jürgensen et al., 2004; Learman et al., 2013; Santelli et al., 2011; Sutherland et al., 2018; Webb et al., 2005), and in marine Fe-Mn oxide deposits (Manceau et al., 2014; Marcus et al., 2004). The changes in Mn redox state are not readily explained by secular changes in dissolved O_2 concentration of the ambient seawater. As previously mentioned, the deposition of CD29 began at ~1,000 m water depth (Horner et al., 2015). In typical seawater, the dissolved O_2 concentration typically reaches a minimum near ~1,000 m from respiration of exported organic carbon from the surface ocean. The thermal subsidence that delivered CD29 to depths near 2,000 m most likely carried CD29 toward more oxygen-ventilated deep water. This presumed history of dissolved O_2 concentration (i.e., increasing over time) is at odds with more oxidized Mn down section in the crust. This indicates that whatever physical, chemical, or biological process that preceded the precipitation of individual growth columns in CD29 produced Mn oxides that contain substantial amounts of Mn(III). The more oxidized outer edges of the growth columns also hint at oxidation resulting from greater exposure to oxygen-bearing pore waters (Figure 9).

A uniformitarian interpretation of EXAFS data collected from CD29 suggests that Mn precipitates as a complex mixture of phases in ferromanganese crusts, which undergo transformations to a more stable oxide phase over several million years. Bulk EXAFS shows a trend of increasing vernadite (δ-MnO_2) with depth from a starting mixture of birnessite, feitknechtite, and asbolane based on the model compounds used (Figure 6; Table 3). Birnessite, feitknechtite, and asbolane may all contain stoichiometric Mn(III) (Post, 1999). Consistent with this is a clear difference in Mn(III) content and mineralogy in different regions of the crust, wherein the uppermost crust has high Mn(III) and high asbolane and feitknechtite components, while the bottom 74.5–105 mm interval is primarily Mn(IV) (>90 mol%) and consists primarily of a hexagonal phyllomanganate (as δ-MnO_2 and acid birnessite). μ-EXAFS data demonstrate significant spatial heterogeneity within this overall trend. The first millimeter of new crust growth contains birnessite (hexagonal), sodium birnessite (triclinic), feitknechtite, and asbolane. Over several millimeters of crust, these initial phases give way to a mixture of vernadite (δ-MnO_2) (hexagonal), acid birnessite (hexagonal), and asbolane with instances of feitknechtite. This general agreement between the bulk and μ-EXAFS data provides some validation for the general, stratigraphic trends. These two measurements together suggest that the mixture of

Table 6
Mn Micro-Extended X-ray Absorption Fine Structure (EXAFS) Fitting Results

Depth in CD-29 (mm)	Description	Mn EXAFS component fits (fraction)					
		δ-MnO_2	Acid birnessite	Sodium birnessite	Feitknechtite	Asbolane	χ_ν^2
0.24	Center of high-Mn growth column	-	0.150	0.192	0.232	0.426	
0.54	High-Fe crack between new growth columns	0.058	0.153	0.256	0.239	0.295	0.178
3.51	High-Fe region on edge of growth column	0.096	0.144	0.210	-	0.551	0.991
13.02	Center of high-Mn growth column	0.344	0.183	-	0.130	0.342	0.275
13.38	High-Fe region on edge of growth column	-	0.464	-	0.104	0.432	0.393
16.41 a	Center of high-Mn growth column	0.282	0.242	-	0.120	0.356	0.196
16.41 b	High-Fe region on edge of growth column	0.170	0.342	-	-	0.487	0.507
79.05	Center of growth structure in phosphatized section of the crust	0.317	0.191	-	0.072	0.419	0.296
79.44	Transition between columnar growth and exsolution bands (high Mn)	0.365	0.311	-	-	0.324	0.447
80.58	Exsolution bands (high Mn)	0.288	0.281	-	-	0.432	0.505
80.79	Transition between columnar growth and exsolution bands (high Fe)	0.241	0.165	0.082	0.182	0.330	0.245
84.39	Exsolution bands (high Mn)	0.379	0.197	-	-	0.424	0.266

hexagonal phyllomanganates observed down crust may form from a recrystallization of primary disordered phases over several millimeters of ferromanganese crust.

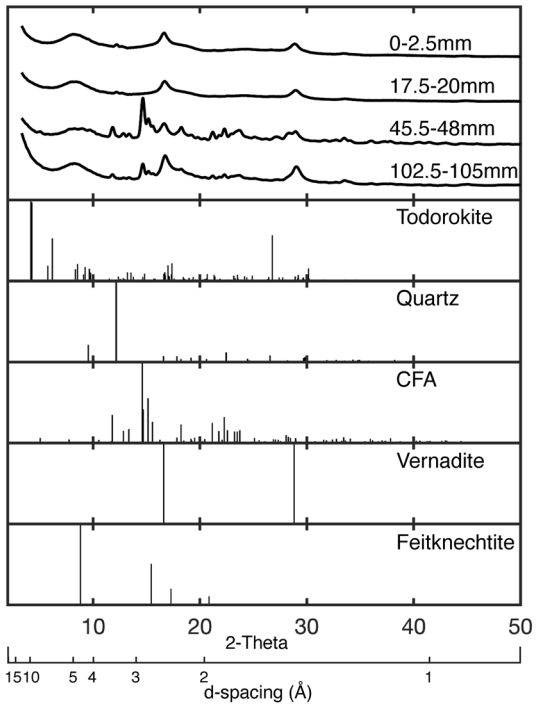

Figure 8. Bulk X-ray powder diffraction (Mo source, λ = 0.70930Å) of samples from CD29 including the surface, 17.5–20, 45.5–48 mm (first appearance of carbonate fluorapatite [CFA]), and the bottom of the crust. Relevant X-ray diffraction standards are also included.

The Mn mineralogy exhibits an increase in vernadite with increasing depth in CD29. We also identified a Mn(III) oxyhydroxide phase, feitknechtite, in the upper sections of the crust that decreases with depth. This observation may indicate that Mn(III) oxyhydroxide is initially deposited as a primary phase, and underwent a diagenetic phase change to vernadite with age. This is somewhat at odds with previous XRD-based observations of ferromanganese deposits that typically consider vernadite as the primary Mn-oxide phase (Dymond et al., 1984; Frank et al., 1999). Previous XRD studies on this very same crust, CD29, concluded that the only Mn-oxide phase present is vernadite. Our XRD measurements of CD29 yielded peaks at ~2.5 and ~1.5 Å, which can be attributed to several Mn oxides, including vernadite and other birnessite minerals, but in the absence of a basal reflection is typically attributed exclusively to vernadite (Frank et al., 1999; Post, 1999). In addition to these peaks, our XRD data also show a broad XRD peak centered at 4.8 Å. This is not readily attributable to any mineral that has been previously identified in CD29. It is close to a 4.6 Å peak expected for feitknechtite, however, lower intensity peaks of feitknechtite (2.69, 2.38, and 1.85 Å) are either not present or not clearly distinguished from the broad vernadite peaks (Figure 8) (Grangeon et al., 2017). The EXAFS spectral fits coupled with the high Mn(III) fraction observed in the XRF redox maps indicate that a poorly crystalline Mn(III) oxyhydroxide phase, possibly feitknechtite, is a predominant phase in this ferromanganese crust. This Mn(III) phase likely transitions to vernadite on million-year time scales. This Mn(III) phase likely transitions to vernadite on million-year time scales.

Despite the persistent presence of birnessite-group minerals indicated with bulk and μ-EXAFS, a basal reflection at 7 or 10 Å was not observed in our bulk XRD analysis. This lack of reflections at 7 and 10 Å does

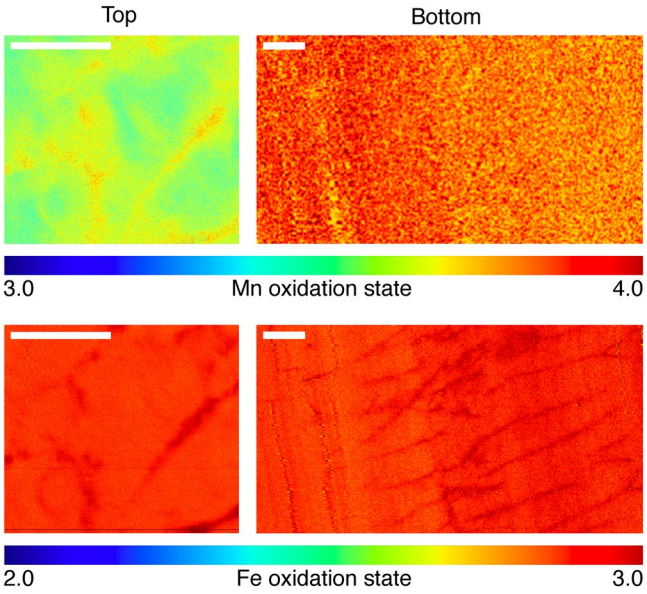

Figure 9. Mn (top) and Fe (bottom) maps of oxidation state determined from multiple-energy mapping (see Materials and Methods) for representative sections from the top (left) and bottom (right) of crust CD29. Mn oxidation state is lower toward the top of the crust and the center of individual growth structures. Fe oxidation state changes little throughout CD29.

not necessarily preclude the presence of these minerals. In fact, a 10 Å Mn oxide was infrequently detected by XRD in other crusts from Karin Ridge (Hein et al., 1990). Vernadite itself lacks a basal reflection (Post, 1999). Previous work offers two possible explanations for this lack of a basal reflection. The first is that vernadite has a turbostratic layer configuration, meaning that sheets of MnO_6 octahedra are rotated and highly disordered in the layer stacking direction (Post, 1999). While this would explain the lack of a basal reflection in vernadite, such an interpretation is not readily applied to minerals that do not have a layered structure, like todorokite, which has a 3 by 3 tunnel structure of MnO_6 octahedra (Post, 1999) (recall that todorokite produces an acceptable EXAFS fit, but was omitted due to poor agreement with previous studies of this same crust and lack of confirmation via XRD). The second explanation put forth to explain the lack of a basal reflection in vernadite is exceedingly small domains of crystallinity. Post (1999) suggested that thin phyllomanganate plates less than 100 Å would be sufficient to preclude Bragg diffraction in the layer-stacking direction. Thus, our findings suggest that previous determinations of Mn-oxide mineralogy in marine Fe-Mn deposits may understate the abundance of other oxide (especially nanocrystalline) minerals when relying on traditional XRD techniques alone (e.g., Frank et al., 1999). While both of these explanations could plausibly explain the high-relative abundance of asbolane that we determined using EXAFS, it is more likely that the significant similarity in the Mn bonding environment (hexagonal MnO_6 sheets) that gives asbolane a very similar EXAFS spectrum to vernadite, and thus is likely overrepresented in our EXAFS fits (Tables 3 and 6) (Post, 1999). Additionally, the relative abundance of Ni and Co in CD29 (~1–2 wt%) is likely insufficient to support such a significant asbolane fraction (Frank et al., 1999; Koschinsky et al., 2020; Manceau et al., 1992b). Therefore, the most parsimonious interpretation of the Mn mineralogy of CD29 includes a primary deposition of a highly disordered phyllomanganate (consisting of mixed hexagonal and triclinic symmetry, mostly as vernadite) and a Mn(III) oxyhydroxide such as feitknechite. This assemblage becomes almost entirely vernadite with depth in the crust.

Nevertheless, the birnessite group of minerals has a wide structural and compositional complexity such that there remains uncertainty as to the level of accuracy in modeling this group using mechanical mixtures of end members (Ling et al., 2018). We pose that combining bulk- and micro-scale analysis for linear combination EXAFS alleviates some uncertainty and provide confirmation of bulk modeling trends. Further, in systems such as Fe-Mn crusts that contain small domains of crystallinity and/or c-disordered crystals, μ-EXAFS tells a much more complex story of early and late mineralogical transformations occurring over the lifetime of the crust.

5. Summary and Conclusions

In this study, we demonstrate the use of μ-XRF, bulk XAS, and μ-XAS to measure major and minor element concentrations in Fe-Mn crust CD29. These components include Mn, Fe, and Si, as well as several transition metals that make up less than 1 weight percent of CD29. The distribution of the major elements suggests that nucleation and growth of this Fe-Mn crust was likely controlled by the availability of Mn and Fe, and detrital silicates and Fe oxides that form around primary Fe-Mn growth columns. We used μ-XRF mapping at multiple energies to measure the two-dimensional redox structure of Mn and Fe in CD29. These maps show that Fe oxidation state has little spatial variation (all around +3), while Mn exhibits average oxidation states from +3.4 to +4.0. The most reduced Mn oxides are present toward the center of growth structures and toward the top of the crust, suggesting that primary Mn oxides formed with an oxidation state of +3.4. Given that this crust likely saw a monotonic increase in the dissolved oxygen of its surrounding seawater, we suggest that higher oxidation states deeper in the crust resulted from post-depositional oxidation. Addi-

tionally, since phosphatization of the older (>47 mm) part of the crust occurred under suboxic conditions, the timing of this post-depositional oxidation is constrained by the episodes of CFA mineralization. Using bulk and μ-EXAFS, we demonstrate that multiple Mn bonding environments exist throughout the crust, including a primary depositional assemblage of disordered phyllomanganates (primarily vernadite), a Mn(III) oxyhydroxide consistent with feitknechtite, and possibly some asbolane. A predominantly vernadite mineralogy in the deeper (older) part of the crust transitions to this mixed Mn-oxide assemblage in the younger crust. We characterized a region of significant post-depositional alteration, which demonstrates features consistent with dissolution and reprecipitation coincident with a Mn oxidation state of approximately +4.0.

Our findings demonstrate the many ways in which the temporal evolution of ferromanganese crusts manifests in oxidation state changes, mineralogy transformations, and element associations, all of which provide context for geochemical studies in ferromanganese materials. For example, the observed Mn redox changes in CD29 suggest that the ability to facilitate oxidative sorption, and potential associated isotopic fractionation, may be altered by post-depositional oxidation of Mn. The consequences of oxidative diagenesis of Mn within Fe-Mn crusts on individual, redox-active metals, likely need to be considered on a case by case basis.

Data Availability Statement

Data have been deposited at Harvard Dataverse and are available for download at the following link: https://doi.org/10.7910/DVN/AIYHIA

Acknowledgments
The authors would like to acknowledge Sune Nielsen (WHOI) for many helpful discussions and Sam Webb for assistance with synchrotron measurements. This research is supported by NASA Exobiology NNX15AM046 to Scott D. Wankel and Colleen M. Hansel, NASA NESSF NNX15AR62H to Kevin M. Sutherland, and WHOI Ocean Exploration Institute to Colleen M. Hansel. The Stanford Synchrotron Radiation Lightsource was utilized in this study. Use of the Stanford Synchrotron Radiation Lightsource, SLAC National Accelerator Laboratory, is supported by the U.S. Department of Energy, Office of Science, Office of Basic Energy Sciences under Contract No. DE-AC02-76SF00515.

References

Banakar, V. K., & Hein, J. R. (2000). Growth response of a deep-water ferromanganese crust to evolution of the Neogene Indian Ocean. *Marine Geology*, *162*(2–4), 529–540. https://doi.org/10.1016/s0025-3227(99)00077-8

Bargar, J. R., Tebo, B. M., & Villinski, J. E. (2000). In situ characterization of Mn (II) oxidation by spores of the marine Bacillus Sp. strain SG-1. *Geochimica et Cosmochimica Acta*, *64*(16), 2775–2778.

Bargar, J. R., Webb, S. M., & Tebo, B. M. (2005). EXAFS, XANES and in-situ SR-XRD characterization of biogenic manganese oxides produced in sea water. *Physica Scripta*, *T115*, 888–890. https://doi.org/10.1238/physica.topical.115a00888

Basu, S., Stuart, F. M., Klemm, V., Korschinek, G., Knie, K., & Hein, J. R. (2006). Helium isotopes in ferromanganese crusts from the central Pacific Ocean. *Geochimica et Cosmochimica Acta*, *70*(15), 3996–4006. https://doi.org/10.1016/j.gca.2006.05.015

Bau, M., Schmidt, K., Koschinsky, A., Hein, J., Kuhn, T., & Usui, A. (2014). Discriminating between different genetic types of marine ferro-manganese crusts and nodules based on rare earth elements and yttrium. *Chemical Geology*, *381*, 1–9. https://doi.org/10.1016/j.chemgeo.2014.05.004

Blöthe, M., Anna, W., Müller, C., Frank, S., Kuhn, T., & Axel, S. (2015). Manganese-cycling microbial communities inside deep-sea manganese nodules. *Environmental Science and Technology*, *49*(13), 7692–7700. https://doi.org/10.1021/es504930v

Bodei, S., Manceau, A., Geoffroy, N., Baronnet, A., & Buatier, M. (2007). Formation of todorokite from vernadite in Ni-rich hemipelagic sediments. *Geochimica et Cosmochimica Acta*, *71*(23), 5698–5716. https://doi.org/10.1016/j.gca.2007.07.020

Bosak, T., Knoll, A. H., & Petroff, A. P. (2013). The meaning of stromatolites. *Annual Review of Earth and Planetary Sciences*, *41*(41), 21–44. https://doi.org/10.1146/annurev-earth-042711-105327

Christensen, J. N., Halliday, A. N., Godfrey, L., Hein, J. R., & Rea, D. K. (1997). Climate and ocean dynamics and the lead isotopic records in pacific ferromanganese crusts. *Science*, *277*, 913–918. https://doi.org/10.1126/science.277.5328.913

Conrad, T., Hein, J. R., Paytan, A., & Clague, D. A. (2017). Formation of Fe-Mn crusts within a continental margin environment. *Ore Geology Reviews*, *87*, 25–40. https://doi.org/10.1016/j.oregeorev.2016.09.010

Crerar, D. A., & Barnes, H. L. (1974). Deposition of deep-sea manganese nodules. *Geochimica et Cosmochimica Acta*, *38*, 279–300.

Cronan, D. S. (1977). Deep-sea nodules: Distribution and geochemistry. *Marine Manganese Deposits*, *15*, 11–44.

Das, S., Jim Hendry, M., & Essilfie-Dughan, J. (2011). Transformation of two-line ferrihydrite to goethite and hematite as a function of PH and temperature. *Environmental Science and Technology*, *45*(1), 268–275. https://doi.org/10.1021/es101903y

Dausmann, V., Frank, M., Siebert, C., Christl, M., & Hein, J. R. (2015). The evolution of climatically driven weathering inputs into the Western Arctic Ocean since the Late Miocene: Radiogenic isotope evidence. *Earth and Planetary Science Letters*, *419*, 111–124. https://doi.org/10.1016/j.epsl.2015.03.007

Dymond, J., Mitchell, L., Finney, B., Piper, D. Z., Murphy, K., Conard, R., & Pisias, N. (1984). Ferromanganese nodules from MANOP sites H, S, and R-control of mineralogical and chemical composition by multiple accretionary processes. *Geochimica et Cosmochimica Acta*, *48*, 931–949. https://doi.org/10.1016/0016-53

Elzinga, E. J. (2011). Reductive transformation of birnessite by aqueous Mn(II). *Environmental Science and Technology*, *45*(15), 6366–6372. https://doi.org/10.1021/es2013038

Farfan, G. A., Amy, A., Webb, S. M., & Hansel, C. M. (2018). Coupled X-ray fluorescence and X-ray absorption spectroscopy for microscale imaging and identification of sulfur species within tissues and skeletons of scleractinian corals. *Analytical Chemistry*, *90*(21), 12559–12566. https://doi.org/10.1021/acs.analchem.8b02638

Frank, M. (2002). Radiogenic isotopes: Tracers of past ocean circulation and erosional input. *Reviews of Geophysics*, *40*(1), 38. https://doi.org/10.1029/2000rg000094

Frank, M., & O'Nions, R. K. (1998). Sources of Pb for Indian Ocean ferromanganese crusts: A record of Himalayan erosion?. *Earth and Planetary Science Letters*, *158*, 121–130. https://doi.org/10.1016/s0012-821x(98)00055-7

Frank, M., O'Nions, R. K., Hein, J. R., & Banakar, V. K. (1999). 60 Myr records of major elements and Pb-Nd isotopes from hydrogenous ferromanganese crusts: reconstruction of seawater paleochemistry. *Geochimica et Cosmochimica Acta*, *63*, 1689–1708. https://doi.org/10.1016/s0016-7037(99)00079-4

Frank, M., Whiteley, N., van de Flierdt, T., Reynolds, B. C., & O'Nions, K. (2006). Nd and Pb isotope evolution of deep water masses in the eastern Indian Ocean during the past 33 Myr. *Chemical Geology*, *226*(3–4), 264–279. https://doi.org/10.1016/j.chemgeo.2005.09.024

Geszvain, K., Butterfield, C., Davis, R. E., Madison, A. S., Lee, S.-W., Parker, D. L., et al. (2012). The molecular biogeochemistry of manganese(II) oxidation. *Biochemical Society Transactions*, *40*(6), 1244–1248. https://doi.org/10.1042/bst20120229

Godfrey, L. V., Lee, D. C., Sangrey, W. F., Halliday, A. N., Salters, V. J. M., Hein, J. R., & White, W. M. (1997). The Hf isotopic composition of ferromanganese nodules and crusts and hydrothermal manganese deposits: Implications for seawater Hf. *Earth and Planetary Science Letters*, *151*, 91–105. https://doi.org/10.1016/S0012-821X(97)00106-4

Grangeon, S., Bruno, L., Miyata, N., Tani, Y., & Manceau, A. (2010). Structure of nanocrystalline phyllomanganates produced by freshwater fungi. *American Mineralogist*, *95*(11–12), 1608–1616. https://doi.org/10.2138/am.2010.3516

Grangeon, S., Warmont, F., Tournassat, C., Bruno, L., Lanson, M., Elkaïm, E., & Claret, F. (2017). Nucleation and growth of feitknechtite from nanocrystalline vernadite precursor. *European Journal of Mineralogy*, *29*(4), 767–776. https://doi.org/10.1127/ejm/2017/0029-2665

Grotzinger, J. P., & Rothman, D. H. (1996). An abiotic model for stromatolite morphogenesis. *Nature*, *383*, 423–425. https://doi.org/10.1038/383423a0

Hansel, C. M. (2017). Manganese in marine microbiology. In R. K. Poole (Ed.), *Advances in microbial physiology* (pp. 37–83). Oxford, UK: Academic Press. https://doi.org/10.1016/bs.ampbs.2017.01.005

Hansel, C. M., Benner, S. G., Jim N., Dohnalkova, A., Kukkadapu, R. K., & Scott, F. (2003). Secondary mineralization pathways induced by dissimilatory iron reduction of ferrihydrite under advective flow. *Geochimica et Cosmochimica Acta*, *67*(16), 2977–2992. https://doi.org/10.1016/S0016-7037(03)00276-X

Hansel, C. M., Benner, S. G., Peter, N., & Scott, F. (2004). structural constraints of ferric (hydr)oxides on dissimilatory iron reduction and the fate of Fe(II). *Geochimica et Cosmochimica Acta*, *68*(15), 3217–3229. https://doi.org/10.1016/j.gca.2003.10.041

Hansel, C. M., & Learman, D. R. (2015). The geomicrobiology of manganese. In H. L. Ehrlich, D. K. Newman, & A. Kappler (Eds.), *Ehrlich's Geomicrobiology* (pp. 403–452). Boca Raton, FL; London, UK; New York, NY: CRC Press.

Hansel, C. M., Zeiner, C. A., Santelli, C. M., & Webb, S. M. (2012). Mn(II) oxidation by an ascomycete fungus is linked to superoxide production during asexual reproduction. *Proceedings of the National Academy of Sciences of the United States of America*, *109*(31), 12621–12625. https://doi.org/10.1073/pnas.1203885109

Hein, J. R., Herbert, K., Schwab, W. C., Usui Taggart, A., Olson, K. L., Pickthorn, L. G., et al. (1990). *Mineralogy and geochemistry of Co-rich ferromanganese crusts and substrate rocks from Karin Ridge and Johnston Island, Farnella Cruise F7-86-HW*. U.S. Geological Survey.

Hein, J. R., Konstantinova, N., Mikesell, M., Mizell, K., Fitzsimmons, J. N., Lam, P. J., et al. (2017). Arctic deep water ferromanganese-oxide deposits reflect the unique characteristics of the arctic ocean. *Geochemistry, Geophysics, Geosystems*, *18*(11), 3771–3800. https://doi.org/10.1002/2017GC007186

Hein, J. R., & Koschinsky, A. (2014). Deep-ocean ferromanganese crusts and nodules. *The Treatise on Geochemistry*, *13*, 273–291. https://doi.org/10.1016/B978-0-08-095975-7.01111-6

Hein, J. R., Koschinsky, A., Bau, M., Manheim, F. T., Kang, J.-K., & Roberts, L. (2000). Cobalt-rich ferromanganese crusts in the pacific. In D. S. Cronan (Ed.), *Handbook of marine mineral deposits* (pp. 239–279). Boca Raton, FL: CRC Press.

Hein, J. R., Koschinsky, A., Halbach, P., Manheim, F. T., Bau, M., Kang, J.-K., & Lubick, N. (1997). Iron and manganese oxide mineralization in the pacific. *Geological Society*, *119*, 123–138.

Hein, J. R., Koschinsky, A., & Kuhn, T. (2020). Deep-ocean polymetallic nodules as a resource for critical materials. *Nature Reviews Earth and Environment*, *1*, 158–169. https://doi.org/10.1038/s43017-020-0027-0

Horner, T. J., Williams, H. M., Hein, J. R., Saito, M. A., Burton, K. W., Halliday, A. N., & Nielsen, S. G. (2015). Persistence of deeply sourced iron in the Pacific Ocean. *Proceedings of the National Academy of Sciences of the United States of America*, *112*(5), 1292–1297. https://doi.org/10.1073/pnas.1420188112

Johnson, J. E., Webb, S. M., Ma, C., & Fischer, W. W. (2016). Manganese mineralogy and diagenesis in the sedimentary rock record. *Geochimica et Cosmochimica Acta*, *173*, 210–231. https://doi.org/10.1016/j.gca.2015.10.027

Jung, H. S., & Lee, C. B. (1999). Growth of diagenetic ferromanganese nodules in an oxic deep-sea sedimentary environment, northeast equatorial pacific. *Marine Geology*, *157*, 127–144. https://doi.org/10.1016/S0025-3227(98)00154-6

Jürgensen, A., Widmeyer, J. R., Gordon, R. A., Bendell-Young, L. I., Moore, M. M., & Daryl Crozier, E. (2004). The structure of the manganese oxide on the sheath of the bacterium leptothrix discophora: An XAFS study. *American Mineralogist*, *89*(7), 1110–1118. https://doi.org/10.2138/am-2004-0724

Klemm, V., Levasseur, S., Frank, M., Hein, J. R., & Halliday, A. N. (2005). Osmium isotope stratigraphy of a marine ferromanganese crust. *Earth and Planetary Science Letters*, *238*(1–2), 42–48. https://doi.org/10.1016/j.epsl.2005.07.016

Koschinsky, A., & Hein, J. R. (2003). Uptake of elements from seawater by ferromanganese crusts: Solid-phase associations and seawater speciation. *Marine Geology*, *198*(3–4), 331–351. https://doi.org/10.1016/s0025-3227(03)00122-1

Koschinsky, A., James, R., HeinDennis Kraemer, Foster, A. L., Kuhn, T., & Halbach, P. (2020). Platinum enrichment and phase associations in marine ferromanganese crusts and nodules based on a multi-method approach. *Chemical Geology*, *539*, 119426. https://doi.org/10.1016/j.chemgeo.2019.119426

Koschinsky, A., Stascheit, A., Bau, M., & Halbach, P. (1997). Effects of phosphatization on the geochemical and mineralogical composition of marine ferromanganese crusts. *Geochimica et Cosmochimica Acta*, *61*, 4079–4094. https://doi.org/10.1016/s0016-7037(97)00231-7

Kuhn, T., Anna, W., Rühlemann, C., & Annemiek, V. (2017). Composition, formation, and occurrence of polymetallic nodules. In R. Sharma (Ed.), *Deep-sea mining* (pp. 23–63). Cham, Switzerland: Springer. https://doi.org/10.1007/978-3-319-52557-0_19

Learman, D. R., Voelker, B. M., Madden, A. S., & Hansel, C. M. (2013). Constraints on superoxide mediated formation of manganese oxides. *Frontiers in Microbiology*, *4*, 11. https://doi.org/10.3389/fmicb.2013.00262

Learman, D. R., Voelker, B. M., Vazquez-Rodriguez, A. I., & Hansel, C. M. (2011a). Formation of manganese oxides by bacterially generated superoxide. *Nature Geoscience*, *4*(2), 95–98. https://doi.org/10.1038/ngeo1055

Learman, D. R., Wankel, S. D., Webb, S. M., Martinez, N., Madden, A. S., & Hansel, C. M. (2011b). Coupled biotic-abiotic Mn(ii) oxidation pathway mediates the formation and structural evolution of biogenic Mn oxides. *Geochimica et Cosmochimica Acta*, *75*(20), 6048–6063. https://doi.org/10.1016/j.gca.2011.07.026

Ling, H. F., Burton, K. W., O'Nions, R. K., Kamber, B. S., von Blanckenburg, F., Gibb, A. J., & Hein, J. R. (2002). Evolution of Nd and Pb isotopes in central pacific seawater from ferromanganese crusts. *Earth and Planetary Science Letters*, *146*(1–2), 1–12. https://doi.org/10.1016/S0012-821X(96)00224-5

Ling, F. T., Post, J. E., Heaney, P. J., & Ilton, E. S. (2018). The relationship between Mn oxidation state and structure in triclinic and hexagonal birnessites. *Chemical Geology*, *479*, 216–227. https://doi.org/10.1016/j.chemgeo.2018.01.011

Madison, A. S., Tebo, B. M., Alfonso Mucci, Sundby, B., & Luther, G. W. (2013). Abundant porewater Mn(III) is a major component of the sedimentary redox system. *Science*, *341*(6148), 875–878. https://doi.org/10.1126/science.1241396

Manceau, A., Gorshkov, A. I., & Drits, V. A. (1992a). Structural chemistry of Mn, Fe, Co, and Ni in manganese hydrous oxides: Part I. Information from XANES spectroscopy. *American Mineralogist*, *77*, 1133–1143.

Manceau, A., Gorshkov, A. I., & Drits, V. A. (1992b). Structural chemistry of Mn, Fe, Co, and Ni in manganese hydrous oxides: Part II. Information from EXAFS spectroscopy and electron and X-ray diffraction. *American Mineralogist*, *77*, 1144–1157.

Manceau, A., Kersten, M., Marcus, M. A., Geoffroy, N., & Granina, L. (2007a). Ba and Ni speciation in a nodule of binary Mn oxide phase composition from Lake Baikal. *Geochimica et Cosmochimica Acta*, *71*(8), 1967–1981. https://doi.org/10.1016/j.gca.2007.02.007

Manceau, A., Lanson, M., & Geoffroy, N. (2007b). Natural speciation of Ni, Zn, Ba, and As in ferromanganese coatings on quartz using X-ray fluorescence, absorption, and diffraction. *Geochimica et Cosmochimica Acta*, *71*(1), 95–128. https://doi.org/10.1016/j.gca.2006.08.036

Manceau, A., Lanson, M., & Takahashi, Y. (2014). Mineralogy and crystal chemistry of Mn, Fe, Co, Ni, and Cu in a deep-sea pacific polymetallic nodule. *American Mineralogist*, *99*(10), 2068–2083. https://doi.org/10.2138/am-2014-4742

Manceau, A., Tamura, N., Celestre, R. S., MacDowell, A. A., Geoffroy, N., Garrison, S., & Padmore, H. A. (2003). Molecular-scale speciation of Zn and Ni in soil ferromanganese nodules from loess soils of the Mississippi basin. *Environmental Science and Technology*, *37*(1), 75–80. https://doi.org/10.1021/es025748r

Marcus, M. A., Edwards, K. J., Gueguen, B., & Fakra, S. C. Gregory H., Jelinski, N. A., et al. (2015). Iron mineral structure, reactivity, and isotopic composition in a South Pacific gyre ferromanganese nodule over 4Ma. *Geochimica et Cosmochimica Acta*, *171*, 61–79. https://doi.org/10.1016/j.gca.2015.08.021

Marcus, M. A., Manceau, A., & Kersten, M. (2004). Mn, Fe, Zn and As Speciation in a fast-growing ferromanganese marine nodule. *Geochimica et Cosmochimica Acta*, *68*(14), 3125–3136. https://doi.org/10.1016/j.gca.2004.01.015

Marcus, M. A., Toner, B. M., & Takahashi, Y. (2018). Forms and distribution of Ce in a ferromanganese nodule. *Marine Chemistry*, *202*, 58–66. https://doi.org/10.1016/j.marchem.2018.03.005

Mayhew, L. E., Webb, S. M., & Templeton, A. S. (2011). Microscale imaging and identification of Fe speciation and distribution during fluid-mineral reactions under highly reducing conditions. *Environmental Science and Technology*, *45*(10), 4468–4474. https://doi.org/10.1021/es104292n

Nielsen, S. G., Mar-Gerrison, S., Gannoun, A., LaRowe, D., Klemm, V., Halliday, A. N., et al. (2009). Thallium isotope evidence for a permanent increase in marine organic carbon export in the early Eocene. *Earth and Planetary Science Letters*, *278*(3–4), 297–307. https://doi.org/10.1016/j.epsl.2008.12.010

Nielsen, S. G., Wasylenki, L. E., Rehkamper, M., Peacock, C. L., Xue, Z. C., & Moon, E. M. (2013). Towards an understanding of Thallium isotope fractionation during adsorption to manganese oxides. *Geochimica et Cosmochimica Acta*, *117*, 252–265. https://doi.org/10.1016/j.gca.2013.05.004

Ohta, A., & Kawabe, I. (2001). REE(III) adsorption onto Mn dioxide (Delta-MnO_2) and Fe oxyhydroxide: Ce(III) oxidation by Delta-MnO_2. *Geochimica et Cosmochimica Acta*, *65*, 695–703. https://doi.org/10.1016/s0016-7037(00)00578-0

Oldham, E., Alfonso, M., Tebo, B. M., & Luther, G. W. (2017). ScienceDirect soluble Mn (III)–L complexes are abundant in oxygenated waters and stabilized by humic ligands. *Geochimica et Cosmochimica Acta*, *199*, 238–246. https://doi.org/10.1016/j.gca.2016.11.043

Peacock, C. L., & Moon, E. M. (2012). Oxidative scavenging of thallium by birnessite: Explanation for thallium enrichment and stable isotope fractionation in marine ferromanganese precipitates. *Geochimica et Cosmochimica Acta*, *84*, 297–313. https://doi.org/10.1016/j.gca.2012.01.036

Peacock, C. L., & Sherman, D. M. (2007). Crystal-chemistry of Ni in marine ferromanganese crusts and nodules. *American Mineralogist*, *92*(7), 1087–1092. https://doi.org/10.2138/am.2007.2378

Post, J. E. (1999). Manganese oxide minerals: crystal structures and economic and environmental significance. *Proceedings of the National Academy of Sciences of the United States of America*, *96*, 3447–3454. https://doi.org/10.1073/pnas.96.7.3447

Puteanus, D., & Halbach, P. (1988). Correlation of Co concentration and growth rate—A method for age determination of ferromanganese crusts. *Chemical Geology*, *69*, 73–85..

Rehkämper, M., Frank, M., Hein, J. R., & Halliday, A. (2004). Cenozoic marine geochemistry of thallium deduced from isotopic studies of ferromanganese crusts and pelagic sediments. *Earth and Planetary Science Letters*, *219*(1), 77–91. https://doi.org/10.1016/S0012-821X(03)00703-9

Rona, P. A. (2008). The changing vision of marine minerals. *Ore Geology Reviews*, *33*(3–4), 618–666. https://doi.org/10.1016/j.oregeorev.2007.03.006

Santelli, C. M., Webb, S. M., Dohnalkova, A. C., & Hansel, C. M. (2011). Diversity of Mn oxides produced by Mn(II)-oxidizing fungi. *Geochimica et Cosmochimica Acta*, *75*(10), 2762–2776. https://doi.org/10.1016/j.gca.2011.02.022

Shiraishi, F., Mitsunobu, S., Suzuki, K., Hoshino, T., Morono, Y., & Inagaki, F. (2016). Dense microbial community on a ferromanganese nodule from the ultra-oligotrophic south pacific gyre: Implications for biogeochemical cycles. *Earth and Planetary Science Letters*, *447*, 10–20. https://doi.org/10.1016/j.epsl.2016.04.021

Sutherland, K. M., Wankel, S. D., & Hansel, C. M. (2018). Oxygen isotope analysis of bacterial and fungal manganese oxidation. *Geobiology*, *16*(4), 399–411. https://doi.org/10.1111/gbi.12288

Sutherland, K. M., Wostbrock, J. A. G., Hansel, C. M., Sharp, Z. D., Hein, J. R., & Wankel, S. D. (2020). Ferromanganese crusts as recorders of marine dissolved oxygen. *Earth and Planetary Science Letters*, *533*, 116057. https://doi.org/10.1016/j.epsl.2019.116057

Takahashi, Y., Manceau, A., Geoffroy, N., Marcus, M. A., & Usui, A. (2007). Chemical and structural control of the partitioning of Co, Ce, and Pb in marine ferromanganese oxides. *Geochimica et Cosmochimica Acta*, *71*(4), 984–1008. https://doi.org/10.1016/j.gca.2006.11.016

Tang, Y. Z., Zeiner, C. A., Santelli, C. M., & Hansel, C. M. (2013). Fungal oxidative dissolution of the Mn(II)-bearing mineral rhodochrosite and the role of metabolites in manganese oxide formation. *Environmental Microbiology*, *15*(4), 1063–1077. https://doi.org/10.1111/1462-2920.12029

Tebo, B. M., Bargar, J. R., Clement, B. G., Dick, G. J., Murray, K. J., Parker, D., et al. (2004). Biogenic manganese oxides: Properties and mechanisms of formation. *Annual Review of Earth and Planetary Sciences*, *32*, 287–328. https://doi.org/10.1146/annurev.earth.32.101802.120213

Tebo, B. M., Johnson, H. A., McCarthy, J. K., & Templeton, A. S. (2005). Geomicrobiology of manganese(II) oxidation. *Trends in Microbiology*, *13*(9), 421–428. https://doi.org/10.1016/j.tim.2005.07.009

Toner, B., Manceau, A., Webb, S. M., & Garrison, S. (2006). Zinc sorption to biogenic hexagonal-birnessite particles within a hydrated bacterial biofilm. *Geochimica et Cosmochimica Acta*, *70*(1), 27–43. https://doi.org/10.1016/j.gca.2005.08.029

Villalobos, M., Bruno, L., Manceau, A., Toner, B., & Garrison, S. (2006). Structural model for the biogenic Mn oxide produced by pseudomonas putida. *American Mineralogist*, *91*(4), 489–502. https://doi.org/10.2138/am.2006.1925

Villalobos, M., Toner, B., Bargar, J., & Sposito, G. (2003). Characterization of the manganese oxide produced by pseudomonas putida strain MnB1. *Geochimica et Cosmochimica Acta*, *67*(14), 2649–2662. https://doi.org/10.1016/s0016-7037(03)00217-5

von Blanckenburg, F., Belshaw, N. S., & O'Nions, R. K. (1996). Separation of 9Be and cosmogenic 10Be from environmental materials and SIMS isotope dilution analysis. *Chemical Geology*, *129*, 93–99. https://doi.org/10.1016/0009-2541(95)00157-3

Von Stackelberg, U. (2000). Manganese nodules of the Peru basin. In D. S. Cronan (Ed.), *Handbook of Marine Mineral Deposits*. (pp. 197–238). Boca Raton, FL; London, UK; New York, NY; Washington, DC: CRC Press.

Wang, X., Planavsky, N. J., Reinhard, C. T., Hein, J. R., & Johnson, T. M. (2016). A Cenozoic seawater redox record derived from 238U/235U in ferromanganese crusts. *American Journal of Science*, *315*(11), 64–83. https://doi.org/10.2475/01.2016.02

Webb, S. M. (2005). SIXPACK: A graphical user interface for XAS analysis using IFEFFIT. *Physica Scripta*, *T115*, 1011–1014. https://doi.org/10.1238/Physica.Topical.115a01011

Webb, S. M. (2011). The MicroAnalysis Toolkit: X-ray fluorescence image processing software. In *AIP Conference Proceedings*. (Vol. *1365*, pp. 196–199).https://doi.org/10.1063/1.3625338

Webb, S. M., Dick, G. J., Bargar, J. R., & Tebo, B. M. (2005). Evidence for the presence of Mn(III) intermediates in the bacterial oxidation of Mn(II). *Proceedings of the National Academy of Sciences of the United States of America*, *102*(15), 5558–5563. https://doi.org/10.1073/pnas.0409119102

Wegorzewski, A. V., Grangeon, S., Webb, S. M., Heller, C., & Kuhn, T. (2020). Mineralogical transformations in polymetallic nodules and the change of Ni, Cu and Co crystal-chemistry upon burial in sediments. *Geochimica et Cosmochimica Acta*, *282*, 19–37. https://doi.org/10.1016/j.gca.2020.04.012

Wegorzewski, A. V., & Kuhn, T. (2014). The influence of suboxic diagenesis on the formation of manganese nodules in the clarion clipperton nodule belt of the Pacific Ocean. *Marine Geology*, *357*, 123–138. https://doi.org/10.1016/j.margeo.2014.07.004